ORIGINAL RESEARCH ARTICLE

Structural, Optical and Magnetic Properties of Diamagnetic Cd²⁺ Incorporated Cobalt Ferrite Thin Films Deposited by Spray Pyrolysis

Gajanan L. Jadhav[1] · Pankaj P. Khirade[2] ⊕ · Apparao R. Chavan[3] · C. M. Kale[4] · K. M. Jadhav[5]

Abstract

Cadmium (Cd²⁺)-substituted cobalt ferrite thin films with configuration $Co_{1-x}Cd_xFe_2O_4$ ($x = 0.0$ to 1.0 in steps of 0.2) were grown via spray pyrolysis. The influence of Cd^{2+} substitution on structural and functional properties was investigated. X-ray diffraction analysis clearly shows a single-phase cubic spinel geometry (*Fd3m* space group). The ultrafine nanocrystallites with average crystallite dimensions of 11–15 nm were obtained. The surface topography was inspected by scanning electron microscopy. The uniform distribution of the crystallites in nanosize dimensions (10–14 nm) was also supported by transmission electron microscopy. The contact angle measurements of the fabricated thin films demonstrate special affinity towards water molecules. FTIR spectra affirmed the construction of spinel ferrite structure and the band position was influenced by Cd^{2+}-substitution. The optical band gap energy (E_g) can be tuned by Cd^{2+}-substitution and decreases from 2.98 to 2.10 eV viewing the semiconducting performance. The PL investigation showed the distinguishing near-band-edge emission at about 700 nm, which can be ascribed to the re-grouping of electrons with light-produced holes in oxygen vacancies and creation of intrinsic defects. Magnetic properties, i.e. saturation magnetization (M_s, 412.84–111.47 emu/cc), remanence magnetization (M_r, 44.83–2.18 emu/cc) and coercivity (H_c, 402.12–78.12 Oe), decreased with increasing diamagnetic Cd^{2+} substitution due to a decrease in net magnetization.

Keywords Thin film · spray pyrolysis · spinel ferrite · photoluminescence · magnetic properties

Introduction

In the modern era of technology, spinel ferrite materials with striking ferrimagnetic and dielectric characteristics are dominating in electronics. Nanocrystalline spinel ferrites have attracted unusual consideration from scientists in the arena of microelectronic technology and biomedical sciences on account of their supreme electric, dielectric, and magneto-optical properties.[1–3] These diverse properties validate them for many industrial applications such as microwave appliances,[4] transformers,[5] storage instruments,[6] water and wastewater purification,[7] biomedical tools,[8] and spintronic devices.[9]

In the assembly of spinel ferrites, cobalt ferrite ($CoFe_2O_4$) is appealing owing to its different longitudinal magnetization from the transverse, high Curie point temperature (T_c), sensible saturation magnetization, high magnetostriction parameters, and extraordinary thermal and chemical solidity.[10–14] Cobalt ferrite nanocrystals are potential candidates in the biomedical arena as contrast agents in magnetic resonance imaging and in thermally activated cancer therapy,[15] segregation and purification of genomic DNA[16] and the departure of polymerase chain response organized DNA,[17] and particularly in hyperthermia treatments.[18]

Minor variations in the chemical composition can be accomplished by cation exchange or doping with cations. Structural and microstructural modification can be attained by optimization of synthesis routes, synthesis constraints, or stacking with other chemical or biological synthesis routes

✉ Pankaj P. Khirade
  pankajkhirade@gmail.com

1 Department of Physics, Science College, Congress Nagar, Nagpur, MS 440012, India

2 Department of Physics, Shri Shivaji Science College, Amravati, MS 444603, India

3 Department of Physics, Sir Parashurambhau College, Pune, MS 411030, India

4 Indraraj Arts, Commerce and Science College, Sillod, Aurangabad, MS 431112, India

5 Department of Physics, Dr. Babasaheb Ambedkar Marathwada University, Aurangabad, MS 431004, India

such as solid-state reaction, sol-gel, and high energy ball milling.[19,20] These alterations have substantial impacts on the subsequent physicochemical properties and applications of the end materials.[21]

Cadmium (Cd^{2+}) is a silvery metal and is known as a toxic element which causes birth defects and cancer.[22] However, still it has promising applications such as in the production of nickel-cadmium (Ni-Cd) rechargeable batteries,[23,24] as a corrosion-resistant plating on steel,[25] solar cells,[26] plastic stabilizers,[27] and pigments.[28] The literature illustrates that mixed $CdFe_2O_4$ ferrite shows a normal spinel structure with Cd^{2+} ions preferentially located at tetrahedral (A)-site, which modifies the magnetic properties of parent Ni/Co/Zn ferrites.[29–31] Cd-substituted spinel ferrites are industrially imperative materials owing to their high resistivity, high permeability, and reasonably low magnetic losses, so they are more appropriate for electrical switching applications, microwave devices, multilayer chip inducers, computer processors, televisions, and mobile headsets.[32–37]

Rahimi et al.[38] investigated the structural and magnetic properties of Cd-substituted nickel ferrite nanoparticles and observed that the saturation magnetization increases with small Cd concentration ($x = 0.3$) then tends to decrease with higher Cd^{2+} content. The increase in magnetic moment with Cd content was elucidated on the foundation of Neel's two-sublattice collinear model. The magnetic and microwave absorbing properties of combustion-synthesized Ni-Cd nanoferrites were studied by Shelar et al.[39], Rasheed et al.[40] detected an enrichment of electrical and magnetic properties of cobalt ferrite nanocrystals by co-substitution of Li-Cd ions. The structural and infrared spectral properties of Cd-doped cobalt ferrite (via ceramic method) for higher Cd content were studied by Dalawai et al.[41], Kardile et al.[42] reported the outcome of Cd^{2+} incorporation on the structural and magneto-optical properties of nickel ferrite thin films developed through spray pyrolysis route. The sensible saturation magnetization values were obtained with Cd^{2+} -doping and hydrophilic behavior of the grown thin films were observed. However, the optical energy band gap critically decreases from 2.11 to 1.86 eV which was due to Cd^{2+} -doping. The literature survey depicts that the Cd^{2+} -substituted cobalt ferrite in nanostructural dimensions significantly alters the magnetic and magnetostrictive characteristics. The doping of Cd^{2+} ions reduces the Curie temperature and gives cobalt nanoferrite diverse electrical and dielectric characteristics.

Several dynamic approaches to grow thin films of spinel ferrite materials in the development of technology. The thin films of spinel ferrite solids are projected to be a potential contender for forthcoming electrical and microelectronic devices.[43,44] The bulk component of ferrite cannot be used with electronic applications, but ferrite thin films can be employed in microwave integrated circuits and may be used to substitute the surface-mounted devices in the future. For

accuracy in the performance of the thin film-based devices, control over the film properties is essential. Therefore, many efforts have been taken by researchers to deposit spinel ferrite thin films using diverse techniques.[45,46] Among the wet chemical approaches, spray pyrolysis is usually used due to its low cost, simple procedure and production of uniform thin films with larger surface area.[47,48]

In the literature, several reports are presented on the fabrication and investigation of physical properties of pristine and substituted cobalt ferrite thin films along with diverse substituents.[49–51]

In this article, cadmium (Cd^{2+})-incorporated cobalt ferrite thin films with chemical formulation $Co_{1-x}Cd_xFe_2O_4$ (where $x = 0.0, 0.2, 0.4, 0.6, 0.8$ and 1.0) were deposited on pre-heated glass substrate via spray pyrolysis. The investigations on structural, morphological, infrared spectral, wettability, optical (UV–Vis, PL) and magnetic properties of $Co_{1-x}Cd_xFe_2O_4$ thin films are analyzed in this report.

Experimental

Synthesis

The thin films of $Co_{1-x}Cd_xFe_2O_4$ (where $x = 0.0, 0.2, 0.4, 0.6, 0.8$ and 1.0) were deposited on the cleaned glass substrate of dimensions 75 mm × 25 mm × 1.35 mm (using chromic acid, ethanol and acetone) by via spray pyrolysis. Analytical grade (purity ~99.98%) cobalt nitrate ($Co(NO_3)_2.6H_2O$), cadmium nitrate ($Cd(NO_3)_3.9H_2O$) and ferric nitrate ($Fe(NO_3)_3.9H_2O$) were used as reactants. Each nitrate was liquified in deionized water, taking 0.1 molarity of each ion, i.e. Co^{2+}, Cd^{2+} and Fe^{3+}. The organized solutions of cobalt, cadmium and ferric nitrates were mixed together in 1:1:2 volumetric proportions, respectively. The mixed solution of cobalt nitrate, cadmium nitrate and ferric nitrate was then sprayed by a spray gun on preheated glass substrate ~380°C by applying appropriate nozzle pressure (0.22 Pa). The scheduled spraying of the solution on the substrate slightly reduces its temperature and it needs around 2–4 min to attain the desired temperature after each spray. The temperature of the substrate was sustained utilizing a temperature controller. A suitable thermocouple of chromel-alumel was used to measure the substrate temperature. The values of various optimized parameters such as spray pressure, nozzle-to-substrate distance, and spray rate were maintained throughout the deposition of thin films and are listed in Table I. The temperature of the substrate was kept constant for 15–20 min after the whole deposition to grow the thin films and further cooled gradually to room temperature. The deposited thin films are finally annealed at 550°C for 3 h, so as to achieve the well crystalline nature in the fabricated thin films and to eliminate the secondary phases grown in the films.

Table I. Optimized parameters of spray deposition of $Co_{1-x}Cd_xFe_2O_4$ (0.0–1.0) thin films

Parameters	Specifications
Molarity proportion	1:1
Volume proportion	1:2
Substrate type and dimensions	Cleaned glass (75 mm × 25 mm × 1.35 mm)
Nozzle to substrate distance	28 cm
Spray rate	5 ml/min
Spray pressure	0.25 Pa
Substrate temperature	380°C
Annealing temperature and time	550°C for 3 h

Characterizations

All the annealed thin films were analyzed by x-ray diffraction (XRD) (Ultima IV, Rigaku Corporation, Japan; Cu-K_α radiation) for exploring the phase structure. The XRD diffractograms were documented in the 2θ scale of 20° to 80° with scanning pulse of 0.01°. The exterior morphology and chemical compositional details were carried out with field emission scanning electron microscopy (FESEM, Hitachi S-4800, Japan). The microstructural results were well supported by transmission electron microscopy (TEM, Philips CM-200). The sessile drop procedure was used to determine the contact angle through dropping a micro-level water drop operating a fine nozzle on the film exterior. In the instance of the static contact angle, the placed drop relies on the surface of a solid. The thickness of the fabricated ferrite thin films was analyzed by using AMBIOS, USA XP-I surface profiler. Infrared properties were examined by Perkin-Elmer Fourier transform infrared spectrophotometry (FTIR). The optical band gap was determined using a UV-Vis spectrometer (Perkin-Elmer Lambda 950). Photoluminescence was acquired in a Fluoromax-4CP-0975D-1512-FM spectrofluorometer in the wavelength range 490–800 nm. Magnetic properties (at room temperature) were employed via vibrating sample magnetometer (VSM Lakeshore-7410).

Results and Discussion

Structural Analysis: XRD

The x-ray diffraction (XRD) patterns of $Co_{1-x}Cd_xFe_2O_4$ ($x = 0.0$–1.0) spinel ferrite thin films are shown in Fig. 1a. The XRD diffractograms of all the thin films show peaks at reflecting planes (220), (311), (222), (400), (422), (511), (440) and (533). All these reflective planes have a standard spinel cubic structure. The analysis of XRD patterns exposed that the development of uni-phase cubic spinel structure having *Fd3m* space group without any contamination peak (JCPDS card no. 77-0426).[52] Figure 1b illustrates the shift in 2θ values for the highly intense (311) peak with Cd^{2+} substitution x. The 2θ values shift towards a lower angle with an increase in Cd^{2+} content which may be due to expansion of the unit cell volume (increase in lattice parameter). The maximum intense (311) peak was utilized to determine the average crystallite size by means of the Debye–Scherrer formula.[53] The values of crystallite size remained within the range of 12–15 nm (listed in Table II). The lattice parameter of the nanoferrite thin films is determined by employing interplanar spacing and Miller indices corresponding to each peak of the XRD patterns.[54] The lattice parameters
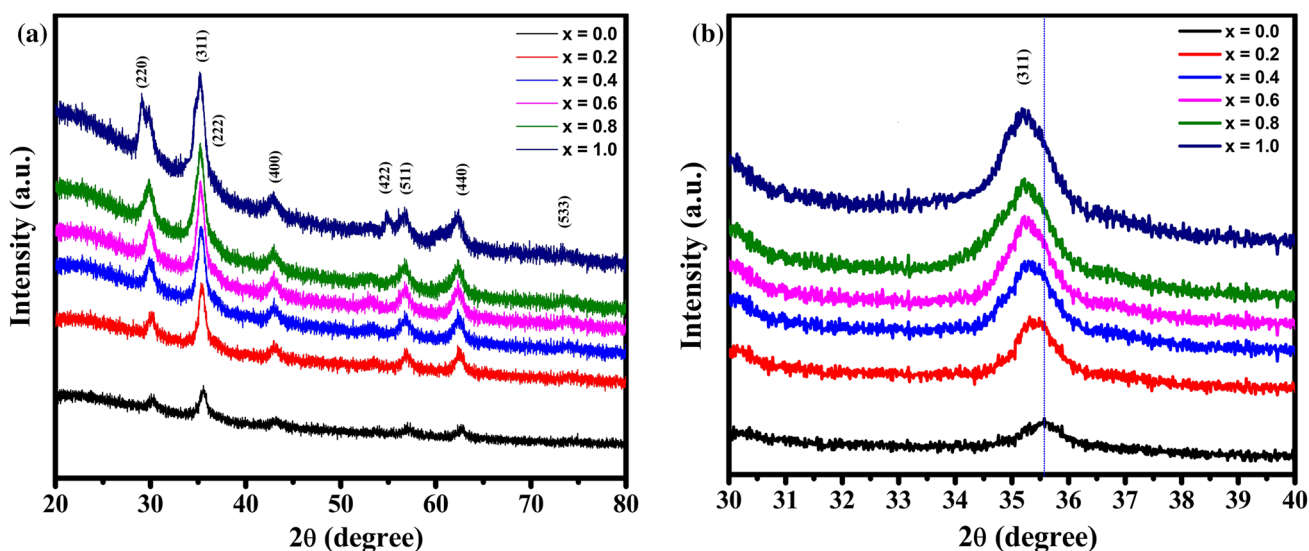

Fig. 1 (a) XRD patterns of $Co_{1-x}Cd_xFe_2O_4$ (0.0–1.0) thin films and (b) Shifting of 2θ angle for the most intense (311) plane.

Table II. Lattice parameter (a), x-ray density (d_{th}), average crystallite size (D) from XRD and t from TEM, thickness of thin film (μ) from surface profiler, absorption band wavenumber (ν) from FTIR of $Co_{1-x}Cd_xFe_2O_4$ ($x = 0.0$–1.0) thin films

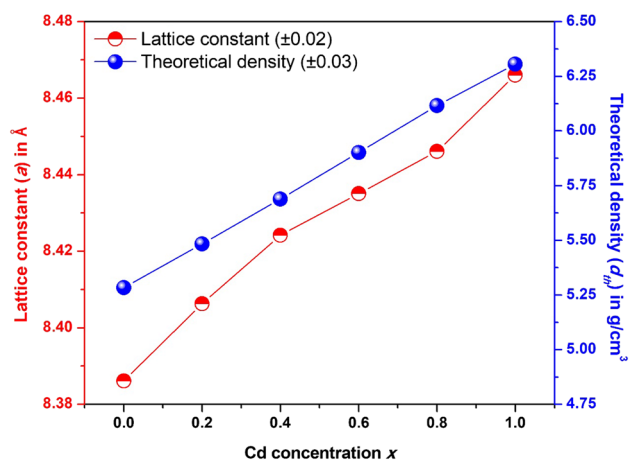| x	a (Å)	d_{th} (g/cm^3)	D (nm) (± 2 nm)	t (nm) (± 1 nm)	μ (nm)	ν (cm^{-1})
0.0	8.386	5.284	12.10	13.12	234	596
0.2	8.406	5.484	13.54	10.25	247	620
0.4	8.424	5.689	11.16	12.24	231	631
0.6	8.435	5.902	11.04	11.03	224	637
0.8	8.446	6.116	11.15	13.54	228	651
1.0	8.466	6.306	15.22	14.53	241	658

Fig. 2 Variation of lattice constant (a) and theoretical density (d_{th}) with Cd^{2+} concentration x.

were found to be between 8.386 Å and 8.466 Å with the upsurge of Cd^{2+} content x. The variation of lattice parameter with Cd^{2+} content x is shown in Fig. 2. From this figure, it is evident that the lattice parameter increases gradually with an increase in Cd^{2+} content. The observed growth in lattice parameter may be attributed to the replacement of smaller ionic radius Co^{2+} (0.78 Å) by larger ionic radii Cd^{2+} (0.97 Å) ions in accordance with Vegard's law.[55] The analogous behaviour of lattice parameter was testified in the literature for Cd^{2+} -doped nickel ferrite.[56]

The theoretical density (d_{th}) of the fabricated thin films was measured utilizing the values of the unit cell volume and molecular weights.[57] The values of d_{th} are tabulated in Table II and graphically demonstrated in Fig. 2, which clearly shows the growing trend with respect to Cd^{2+} content x. The increase in d_{th} may be because the molar mass of incorporated $Cd = 112.411$ g/mol is heavier than that of residing $Co = 58.93$ g/mol ions.

Morphological Analysis: FESEM and TEM

Figure 3a, b and c shows the FESEM images of the annealed films for typical samples of $Co_{1-x}Cd_xFe_2O_4$ (for $x = 0.0$, 0.6

and 1.0) thin films. From the images it is observed that the surface of the film is smooth and has a uniform spherical morphology and is crack-free. Rather densely populated grains on the surface of the film can be observed. FESEM images indicate that there is a slight impact of Cd^{2+} substitution on the microstructure of cobalt ferrite thin films. Also, it can be seen that the thin films have a homogeneous dispersion on the surface and a spheroidal structure. The average grain sizes of about 29.4 nm, 34.2 nm and 43.5 nm (with accuracy of $\pm$ 2 nm) were found for $x = 0.0$, 0.6 and 1.0 thin films, respectively.

Figure 4a and b depicts the bright field TEM images of characteristic $x = 0.0$ and $x = 1.0$ thin film samples, respectively. The images show that the surface is a collection of homogeneously dispersed mono- and partially polycrystalline, faceted crystallites of variable dimensions. The crystallites reveal the agglomerated sphere-shaped and cubical outline morphology for the fabricated samples. The growth speed of these nanoparticles generally depends on the concentration of the raw materials along with deposition kinetics. The average crystallite size (t) was obtained to be in the scale of 12–15 nm, which are consistent with XRD outcomes.

Wettability Properties

The contact angle values permit us to explore the exterior of the fabricated thin films by means of the hydrophilicity or hydrophobicity features.[58] It has been reported that the wettability characteristics of thin film surfaces is chiefly due to both their stoichiometry and microstructure.[59,60] In this study, the contact angles of the fabricated thin films were determined with the sessile drop method via dropping micro-level water droplets by means of an acute needle on the film's exterior.[61] Figure 5 displays the contact angle images of the fabricated thin films. The values of the contact angles (θ) were estimated from Young's formula[62] and are presented in Table III. The contact angles for the entire thin films ranges from 27° to 54°, which shows the hydrophilic (water loving) behaviour. The surface energy assessed from contact angles varies in the range of 51–65 mJ/m^2 (Table III).
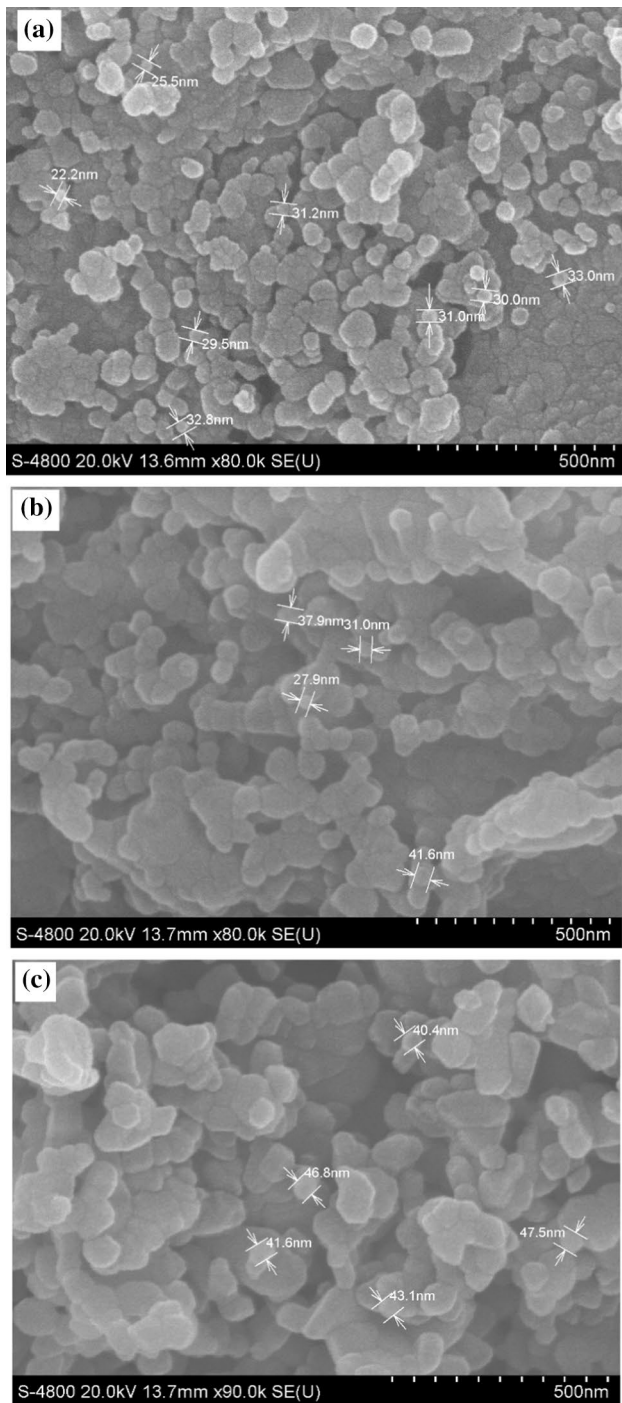
Fig. 3 FESEM images of the $Co_{1-x}Cd_xFe_2O_4$ for (a) $x=0.0$, (b) 0.6 and (c) 1.0 thin films.

Generally, the thickness of the thin films relies on the synthesis method and synthesis parameters viz. dopant concentration, frequency of deposition, deposition temperature and deposition time period. The thickness of the fabricated thin films was measured by a surface profiler.
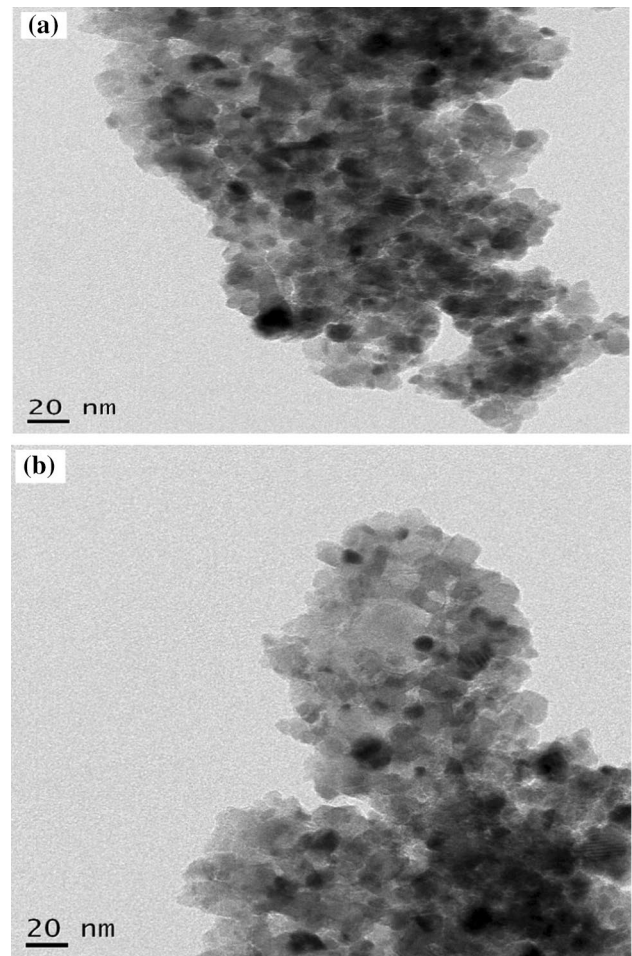

Fig. 4 Representative TEM images for (a) $x=0.0$ and (b) $x=1.0$ thin films.

The thickness of the present thin films was on the order of nanometers (224–247 nm) as given in Table II.

Infrared Spectral (FTIR) Analysis

Figure 6 shows the FTIR transmission spectra of the Cd^{2+} substituted cobalt ferrite thin films. Generally, spinel ferrites exhibit the two main broad metal–oxygen bands attributed to the stretching vibration of M–O as described by Waldron.[63] The intrinsic stretching vibration bands of the metal were mostly detected at the tetrahedral site at 600–550 cm^{-1} and the octahedral widening site at 450–385 cm^{-1}.[64–66] Generally, in spinel ferrites the bond length of the metal-oxygen at tetrahedral site is significantly shorter than that of the octahedral site and thus the higher stretching frequency for the M–O bond at tetrahedral site.[67,68]

However, in the current circumstance only a unique major band near 600 cm^{-1} was observed as the FTIR spectra were documented in the range of 500–4000 cm^{-1}. The value of the major absorption band (ν) for all the thin film
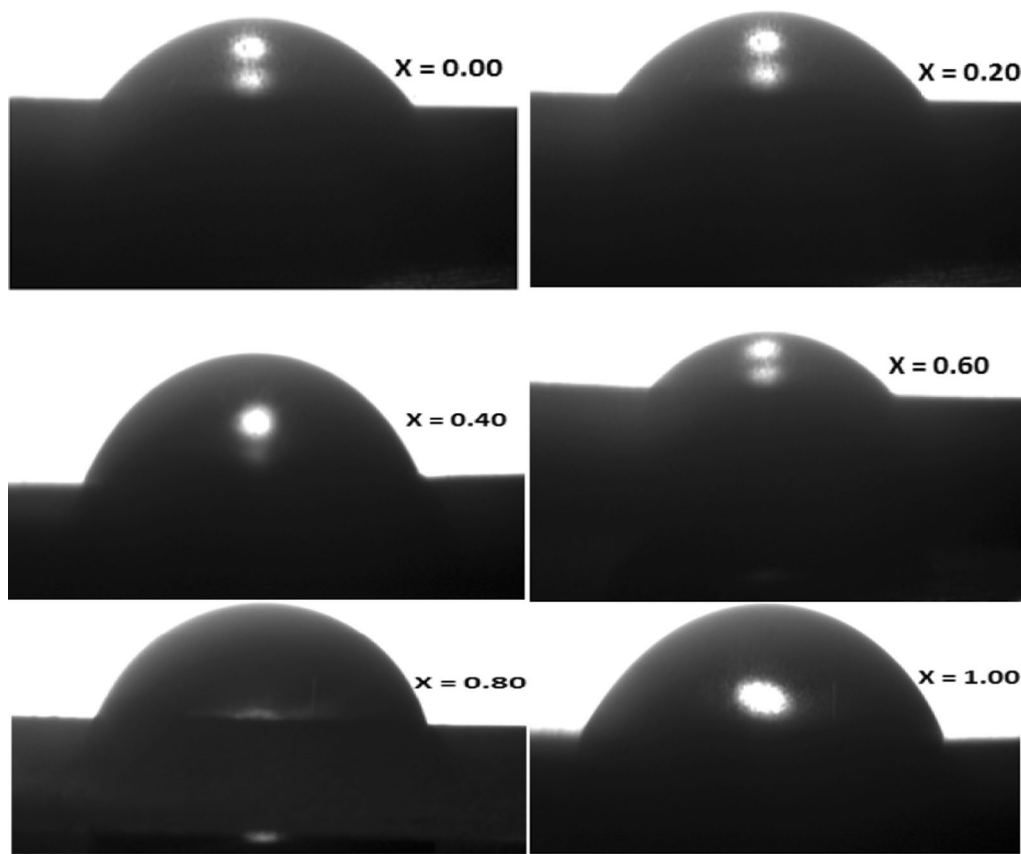
Fig. 5 Images of water droplets on the hydrophilic $Co_{1-x}Cd_xFe_2O_4$ (0.0–1.0) thin films.

Table III. Energy band gap (E_g) from UV–Vis spectroscopy, average contact angle (θ) and surface energy (E_s) from contact angle measurement, saturation magnetization (M_s), remanence magnetization (M_r) and coercivity (H_c) from M–H plots of $Co_{1-x}Cd_xFe_2O_4$ (0.0–1.0) thin films

x	E_g (eV)	θ (°)	E_s (mJ/m^2)	M_S (emu/cc)	M_r (emu/cc)	H_c (Oe)
0.0	2.98	43.44	57.49	412.84	44.83	402.12
0.2	2.65	27.57	65.61	271.00	23.11	291.23
0.4	2.45	54.42	51.17	252.53	16.58	247.61
0.6	2.31	36.26	61.36	191.54	14.59	172.09
0.8	2.25	51.90	52.66	172.95	7.250	116.90
1.0	2.10	52.93	52.05	111.47	2.183	78.12

samples is given in Table II. Additional band appearing near 3500 cm^{-1} could be ascribed to the O-H elongating vibration of water fragments. The band nearby 1550 cm^{-1} resembles anti-symmetric NO$_3$ elongating vibrations and the band at 1647 cm^{-1} corresponds to carboxylate anions.[69] The stretching vibration at 2350 cm^{-1} corresponds to the hydroxyl group. The visibility of absorption bands in the infrared spectra rests on the distribution and type of cations amongst octahedral and tetrahedral sites. With an increase in Cd^{2+} content from $x = 0.0$ to 1.0 the wavenumber of the major band increases from 596 to 658 cm^{-1}. This confirms that the substitution of the cadmium ion changes the inner structure at micro-dimensions due to

variation in ionic radii.[70] Analogously, FTIR results were observed for Cd^{2+}-doped Co-Zn ferrites.[71]

Optical Properties: UV–Visible Spectroscopy (UV–Vis) and Photoluminescence (PL) Spectroscopy

The optical properties of the present Cd^{2+}-incorporated cobalt ferrite thin films were elucidated using UV–Vis spectroscopy. UV–Vis spectra of all the thin films were recorded in the wavelength range of 400–1000 nm at 300 K as depicted in Fig. 7a. The actual absorbance of the thin films was determined by subtracting the standard absorbance value of the glass ingredients, by referring the standard
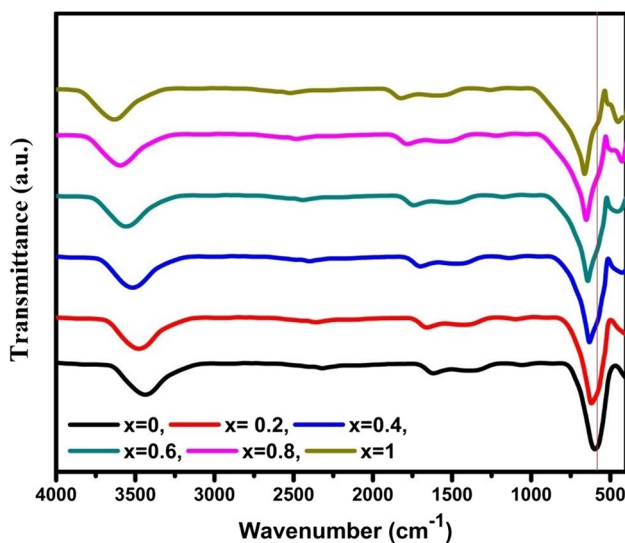
Fig. 6 FTIR spectra of $Co_{1-x}Cd_xFe_2O_4$ (0.0–1.0) thin films.

absorbance data of the glass substrate. Tauc's formula was used to estimate the optical energy band gap (E_g) of all the thin films.[72,73] The optical band gap of the thin films was evaluated by drawing the graph of $(\alpha h\nu)^{1/n}$ versus $h\nu$ and obtaining the intercept of the drawn straight line on the x-axis (Fig. 7b). Between all the values of n, the optimum fit was obtained for the values of $n = \frac{1}{2}$ and $\frac{1}{4}$. The optical energy band gap (E_g), calculated from the Tauc plots range between 2.98 and 2.10 eV. It is evident from Table III that the energy band gap values decrease with an increase in Cd^{2+}-substitution in parent cobalt ferrite thin films. The band gap values of all the thin films depend on numerous factors such as the occurrence of impurities, average crystallite size, film thickness, and lattice strain.[74,75] This reduction in the energy band gap may be attributed to the increased crystallization of the thin films and lessening the crystalline defects which results in the reduction of the number of energy levels amid the valence band and the conduction band.[76] With the substitution of Cd^{2+} ions, Cd^{2+} ions replace the (A) site Co^{2+} ions which can generate impurity bands inside the gap. Once the Cd^{2+} concentration is lower, the parting between the valence band and the bottommost impurity band become effective band structures. As the Cd^{2+} dopant concentration increases, the widths of these impurity bands increase, and these bands may overlap together accounting for lessening in band gap energy (Table III). The obtained optical band gap energy for pure cobalt ferrite is found to be in the reported range.[77]

The photoluminescence (PL) spectroscopy is an exceptional method to clarify valuable facts about energy along with changing aspects of charge transporters produced throughout the introduction of light.[78] In spinel ferrites, electrons are located in trap states, excitonic states and
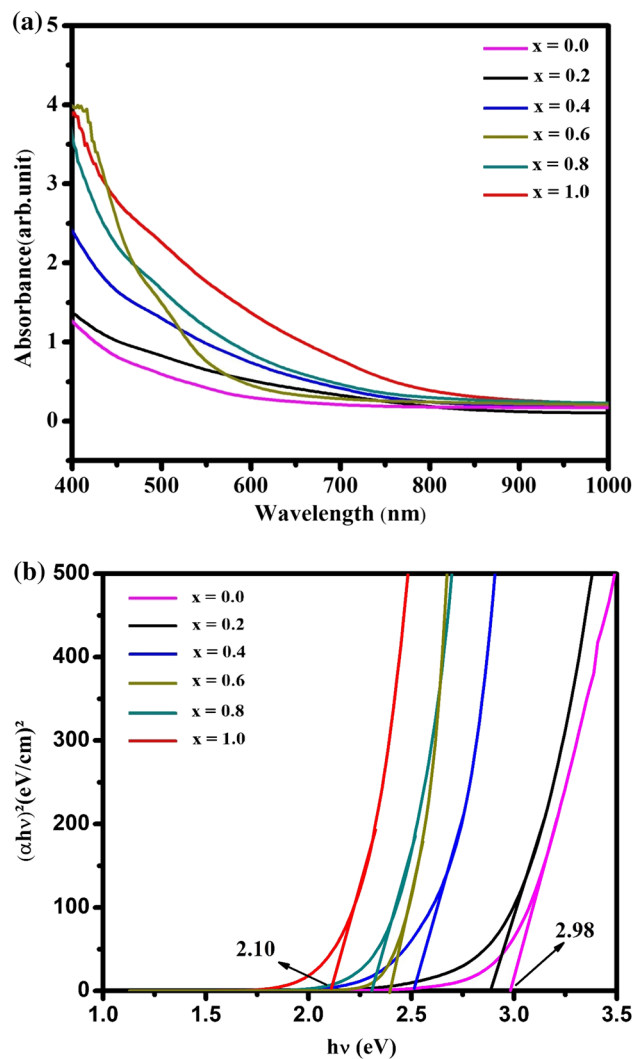

Fig. 7 (a) UV–Vis absorption spectra for $Co_{1-x}Cd_xFe_2O_4$ (0.0–1.0) thin films, (b) Tauc plots for $Co_{1-x}Cd_xFe_2O_4$ (0.0–1.0) thin films.

conduction bands. The PL spectrum of Cd^{2+}-incorporated cobalt ferrite thin films (at room temperature) is described in Fig. 8. The photoluminescence (PL) spectra documented at normal temperature with an excitation wavelength of ~480 nm is portrayed in Fig. 8. PL spectra exhibited a wide-ranging peak between 680 and 800 nm centered at ~730 nm which nearly spans the complete area of visible red.

The direct band edge transition is associated with the thickness of the films and deep trap states inside the band gap.[79] The fabricated Cd^{2+}-incorporated cobalt ferrite thin films were excited by using the excitation wavelength at 678 nm. All thin films exhibited a distinctive near band-edge emission (NBE) at around 700 nm as revealed in Fig. 8. The wider peak shifts towards higher wavelength edge with an increase in Cd^{2+} content. Also, the PL intensity for lower Cd^{2+} content, i.e. $x = 0.2$ and 0.4 samples decrease, while intensity increases significantly for higher Cd^{2+} content
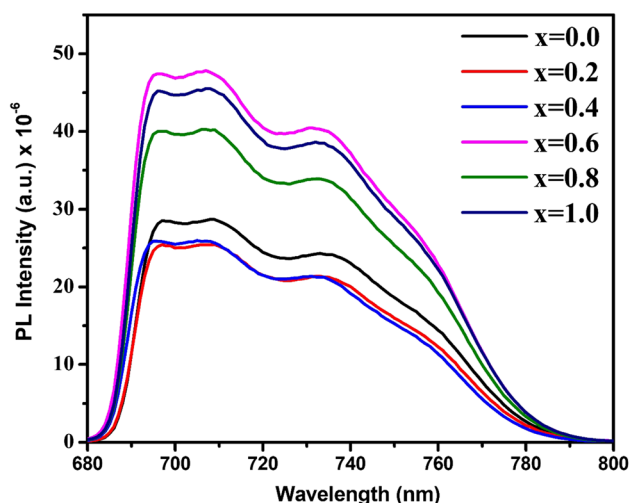
Fig. 8 Photoluminescence spectra for the $Co_{1-x}Cd_xFe_2O_4$ (0.0–1.0) thin films.

Fig. 9 M–H plots of $Co_{1-x}Cd_xFe_2O_4$ (0.0–1.0) thin films.

(i.e. $x = 0.6 – 1.0$) samples. The extensive emission peak in a visible section (~ 680 nm) was found for all samples which is ascribed to the re-grouping of electrons with photo-produced holes imprisoned in oxygen vacancies. This may be attributed to the presence of electronic levels among the conduction and the valence band owing to the increase in intrinsic defects. Consequently, such defects can account for the luminescent characteristics of the fabricated thin films.[80] Comparable PL properties were observed for Mg^{2+} -doped cobalt ferrite thin films in our previous work.[81]

Magnetic Properties

Room temperature magnetic hysteresis loops (M–H) of Cd^{2+} -substituted cobalt ferrite thin films recorded by means of VSM are shown in Fig. 9. The M–H plots verified a typical S-shaped hysteresis loops representing that the sample had a ferromagnetic nature. The values of satura-tion magnetization (M_s), coercivity (H_c) and a remanence magnetization (M_r) were obtained from the M–H loops and are listed in Table III. Likewise, the high values of M_s and H_c designate a nanocrystalline dimensions of the fabricated thin films. Also, it can be observed that all the magnetic parameters (M_s, M_r and H_c) decrease with an increase in Cd^{2+} concentration. The optimal magnetic parameters $M_s = 412.84$ emu/cc and $H_c = 402.12$ Oe were observed for pure cobalt ferrite ($x = 0.0$) thin film. The decrease in magnetic parameters can be attributed to the substitution of diamagnetic Cd^{2+} ions in place of magnetic Co^{2+} ions. The decrease in coercivity may be attributed to the variation in crystallite size with the substitution of Cd^{2+} ions. Generally, in spinel ferrites, three variables of
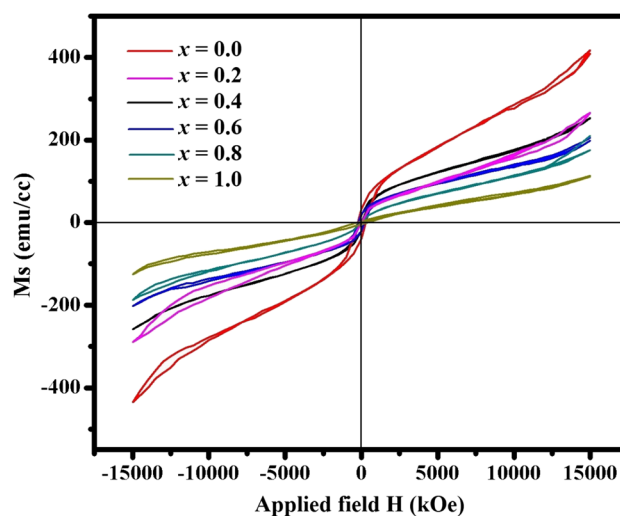
super-exchange communications between the A and B cati-ons of the occupied [A] and [B] sites are convincing for example A-A, B-B then A-B. Also, this A-B interaction was significant because of supreme departures amongst the A-B cations in addition to the bulky degree of dis-tortion between A-B cations with O^{2-} ions. The spins of cations at the occupied [A] and [B] sites magnetize the sub-lattice A and B in a reverse manner and the disparity amid the moments of B and A cations is the total magnetic strength of the spinel ferrite.[82] Therefore, the resulting average saturation magnetization is $M_s = M_B − M_A$, where M_A and M_B are the magnetic strength of the occupied [A] and [B] sites.

In the present case, all the magnetic entities of $Co_{1-x}Cd_xFe_2O_4$ thin films decrease as a function of Cd^{2+} concentration x which is connected to the relationship among tetrahedral [A] and octahedral [B] sites. The cobalt ferrite solid possesses an inverse spinel geometry in which Co^{2+} dwellings in octahedral sites and Fe^{3+} ions are identi-cally distributed in tetrahedral and octahedral sites, with their spin in the reverse direction. The magnetic character-istics are significantly influenced because Co^{2+} ($3d^7$) ions have orbital moments of 3.7 μ_B.[83] Conversely, Cd^{2+} ions can exist on both sites, but dominantly favor occupying the octahedral site. The magnetic moment of Cd^{2+} is zero (0 μ_B), so in pure $CdFe_2O_4$ (i.e. $x = 1.0$ sample), magnetic couplings solely originate from the magnetic moment of Fe^{3+} ions (i.e. 5 μ_B).[84] So, the decrease in magnetic parameters can be attributed to the circumstance when non-magnetic Cd^{2+} ions replace ferromagnetic Co^{2+} ions. Similar reports were obtained for Cd^{2+} -doped nickel fer-rite nanoparticles and elucidated on the basis of Neel's two-sublattice model.[85]

Conclusions

In the present study, Cd^{2+}-substituted $CoFe_2O_4$ thin films with chemical formulation $Co_{1-x}Cd_xFe_2O_4$ ($x = 0.0$, 0.2, 0.4, 0.6, 0.8 and 1.0) were effectively deposited on preheated glass substrates using spray pyrolysis. XRD analysis confirmed the creation of monophasic cubic spinel structure with crystallite sizes ranging between 11 nm and 15 nm. The lattice parameter and theoretical density were found to be increased with an increase in Cd^{2+} substitution following Vegard's law. FESEM analysis confirmed the agglomeration of particles on the film with grain size of 29–43 nm. TEM images show uniform crystallites of sizes 11–14 nm. The contact angle determination proved the hydrophilic behaviour of the films when the contact angle is in the range of 27°–54°. FTIR spectra of the samples established the development of spinel ferrite assembly. The optical band gap energy can be simply tuned by Cd^{2+} substitution and its decrease from 2.98 eV to 2.10 eV which can be understood on the basis of the formation of crystalline defects and crystallite size effect. All thin films displayed the distinctive near-band-edge emission at ~ 700 nm. The extensive emission peak in a visible section (~ 680 nm) was found for all the samples which is ascribed to the presence of electronic levels among the conduction and valence bands owing to the increase in intrinsic defects. Magnetic properties of the fabricated thin films demonstrated the reduced values of magnetic entities (M_s, M_r and H_c) with the increase in diamagnetic Cd^{2+} substitution which can be clarified on the basis of net magnetization. In summary, the Cd^{2+} ion significantly influenced the structural, morphological, and magneto-optical characteristics of cobalt ferrite thin films.

References

1. J.D. Adam, L.E. Davis, G.F. Dionne, E.F. Schloemann, and S.N. Stitzer, *IEEE Trans. Microw. Theory Tech.* 50, 721 (2002).
2. M. Saidani, and M.A.M. Gijs, *Appl. Phys. Lett.* 84, 4496 (2004).
3. S.V. Bhandare, A.V. Rajeev Kumar, H.K. Anupama, V.M. Choudhary, and B.S. Jali, *Ceram. Int.* 46, 17400 (2020).
4. H.L. Glass, *Proc. IEEE* 76, 151 (1988).
5. K. Srinivasamurthy, S. Kubrin, S. Matteppanavar, D. Sarychev, P.M. Kumar, H.W. Azale, and B. Rudraswamy, *Ceram. Int.* 44, 9194 (2018).
6. R. Sharma, P. Thakur, P. Sharma, and V. Sharma, *J. Alloys Compd.* 704, 7 (2017).
7. K.K. Kefeni, B.B. Mamba, and T.A.M. Msagati, *Sep. Purif. Technol.* 188, 399 (2017).
8. S. Amiri, and H. Shokrollahi, *Mater. Sci. Eng. C* 33, 1 (2013).
9. M. Tomar, S.P. Singh, O. Perales-Perez, R. Guzman, E. Calderon, and C. Rinaldi-Ramos, *Microelectron. J.* 36, 475 (2005).
10. Q. Song, and Z.J. Zhang, *J. Am. Chem. Soc.* 126, 6164 (2004).
11. L. Ajroudi, N. Mliki, L. Bessais, V. Madigou, S. Villain, and Ch. Leroux, *Mater. Res. Bull.* 59, 49 (2014).
12. P. Anantharamaiah, and P. Joy, *Mater. Lett.* 236, 303 (2019).
13. P. Anantharamaiah, and P. Joy, *Mater. Lett.* 192, 169 (2017).
14. P. Anantharamaiah, and P. Joy, *Physica B* 554, 107 (2019).
15. H.M. Joshi, Y.P. Lin, M. Aslam, P. Prasad, E.A. Schultz-Sikma, R. Edelman, T. Meade, and V.P. Dravid, *J. Phys. Chem. C* 113, 17761 (2009).
16. J. Prodělalová, B. Rittich, A. Španová, K. Petrová, and M.J. Beneš, *J. Chromatogr. A* 1056, 43 (2004).
17. B. Rittich, A. Španová, D. Horák, M. Beneš, L. Klesnilová, K. Petrová, and A. Rybnikář, *Colloids Surf. B* 52, 143 (2006).
18. S.W. Lee, S. Bae, Y. Takemura, I.-B. Shim, T.M. Kim, J. Kim, H.J. Lee, S. Zurn, and C.S. Kim, *J. Magn. Magn. Mater.* 310, 2868 (2007).
19. R. Kambale, K. Song, Y. Koo, and N. Hur, *J. Appl. Phys.* 110, 053910 (2011).
20. K. El-Sayed, M.B. Mohamed, S. Hamdy, and S.S. Ata-Allah, *J. Magn. Magn. Mater.* 423, 291 (2017).
21. D.S. Mathew, and R.S. Juang, *Chem. Eng. J.* 129, 51 (2007).
22. L. Järup, M. Berglund, C.G. Elinder, G. Nordberg, M. Vanter *Scand. J. Work Environ. Health* 24, 1 (1998)
23. M. Freitas, and S.F. Rosalém, *J. Power Sources* 139, 366 (2005).
24. M. Assefi, S. Maroufi, Y. Yamauchi, and V. Sahajwalla, *Curr. Opin. Green Sustain. Chem.* 24, 26 (2020).
25. H. Kim, B.N. Popov, and K.S. Chen, *Corros. Sci.* 45, 1505 (2003).
26. H. Jun, M. Careem, and A.K. Arof, *Renew. Sustain. Energy Rev.* 22, 148 (2013).
27. R. Bian, L. Li, D. Bao, J. Zheng, X. Zhang, J. Zheng, X. Liu, K. Cheng, and G. Pan, *Environ. Sci. Pollut. Res.* 23, 10028 (2016).
28. A. Fargasova, J. Pastierová, and K.J.P.S. Svetkova, *Plant Soil Environ.* 52, 8 (2006).
29. C. Chinnasamy, A. Narayanasamy, N. Ponpandian, R.J. Joseyphus, K. Chattopadhyay, K. Shinoda, B. Jeyadevan, K. Tohji, K. Nakatsuka, and J.H. Greneche, *Scrip. Mater.* 44, 1411 (2001).
30. P. Nordblad, R. Mohan, and S. Mukherjee, *J. Magn. Magn. Mater.* 441, 710 (2017).
31. M. Gharibshahian, M. Nourbakhsh, and O. Mirzaee, *J. Sol-Gel. Sci. Technol.* 85, 684 (2018).
32. R. Kharabe, R. Devan, and B.K. Chougale, *J. Alloys Compd.* 463, 67 (2008).
33. K. Harish, H.B. Naik, and R. Viswanath, *Catal. Sci. Technol.* 2, 1033 (2012).
34. S. Anjum, H. Tahir, K. Hussain, M. Khaleeq-ur-Rahman, M. Rafique, and S. Naseem, *Physica B* 406, 2555 (2011).
35. A.B. Gadkari, T.J. Shinde, and P.N. Vasambekar, *Sens. Transducers* 137, 145 (2012).
36. M. Karanjkar, N. Tarwal, A. Vaigankar, and P. Patil, *Ceram. Int.* 39, 1757 (2013).
37. K. Hussain, N. Amin, and M.I. Arshad, *Ceram. Int.* 47, 3401 (2020).
38. M. Rahimi, M. Eshraghi, and P. Kameli, *Ceram. Int.* 40, 15569 (2014).
39. M. Shelar, and S.N. Yadav, *Int. J. Self Propag. High Temp. Synth.* 28, 173 (2019).
40. S. Rasheed, R.A. Khan, F. Shah, B. Ismail, J. Nisar, S.M. Shah, A. Rahim, and A.R. Khan, *J. Magn. Magn. Mater.* 471, 236 (2019).
41. S. Dalawai, T. Shinde, A. Gadkari, and P. Vasambekar, *Bull. Mater. Sci.* 36, 919 (2013).

42. H. Kardile, S.B. Somvanshi, A.R. Chavan, A. Pandit, and K.M. Jadhav, *Optik* 207, 164462 (2020).
43. A.R. Chavan, S.D. Birajdar, R.R. Chilwar, and K.M. Jadhav, *J. Alloys Compd.* 735, 2287 (2018).
44. A.R. Chavan, J.S. Kounsalye, R.R. Chilwar, S.B. Kale, and K.M. Jadhav, *J. Alloys Compd.* 769, 1132 (2018).
45. F. Tudorache, P.D. Popa, M. Dobromir, and F. Iacomi, *Mater. Sci. Eng. B* 178, 1334 (2013).
46. C.-Y. Oh, J.-H. Oh, and T. Ko, *IEEE Trans. Mag.* 38, 3018 (2002).
47. D. Perednis, and L.J. Gauckler, *J. Electroceram.* 14, 103 (2005).
48. P.S. Patil, *Mater. Chem. Phys.* 59, 185 (1999).
49. T. Dhakal, D. Mukherjee, R. Hyde, P. Mukherjee, M. Phan, H. Srikanth, and S. Witanachchi, *J. Appl. Phys.* 107, 053914 (2010).
50. G. Dascalu, G. Pompilian, B. Chazallon, V. Nica, O.F. Caltun, S. Gurlui, and C. Focsa, *Appl. Phys. A* 110, 915 (2013).
51. K. Suzuki, T. Namikawa, Y. Yamazaki, and Y. Yamazaki, *Jpn. J. Appl. Phys.* 27, 361 (1988).
52. M. Khandekar, R. Kambale, S. Latthe, J. Patil, P. Shaikh, N. Hur, and S.S. Suryavanshi, *Mater. Lett.* 65, 2972 (2011).
53. A. Raut, P. Khirade, A. Humbe, S. Jadhav, and D.R. Shengule, *J. Supercond. Novel Magn.* 29, 1331 (2016).
54. P.P. Khirade, *J. Nanostruct. Chem.* 9, 163 (2019).
55. A.R. Denton, and N.W. Ashcroft, *Phys. Rev. A* 43, 3161 (1991).
56. R. Verma, S. Kane, P. Tiwari, F. Mazaleyrat, Cd content dependent structural and magnetic properties of Cd-Ni nano ferrite, in AIP Conference Proceedings, AIP Publishing LLC, 2019, pp. 160001
57. P.P. Khirade, S.D. Birajdar, A.V. Humbe, and K.M. Jadhav, *J. Electron. Mater.* 45, 3227 (2016).
58. D. Haydon, and J.L. Taylor, *Nature* 217, 739 (1968).
59. D. Pawar, J. Shaikh, B. Pawar, S. Pawar, P. Patil, and S. Kolekar, *J. Porous Mater.* 19, 649 (2012).
60. J. Plawsky, A. Fedorov, S. Garimella, H. Ma, S. Maroo, L. Chen, and Y. Nam, *Nanoscale Microscale Thermophys. Eng.* 18, 251 (2014).
61. D.N. Staicopolus, *J. Colloid Sci.* 17, 439 (1962).
62. R.J. Good, *J. Am. Chem. Soc.* 74, 5041 (1952).
63. T. Srinivasan, C. Srivastava, N. Venkataramani, and M.J. Patni, *Bull. Mater. Sci.* 6, 1063 (1984).
64. T. Tatarchuk, M. Naushad, J. Tomaszewska, P. Kosobucki, M. Myslin, H. Vasylyeva, and P. Ścigalski, *Environ. Sci. Pollut. Res.* 27, 1–13 (2020).
65. T. Tatarchuk, A. Shyichuk, J. Lamkiewicz, and J. Kowalik, *Ceram. Int.* 46, 14674 (2020).
66. T. Tatarchuk, A. Shyichuk, I. Trawczyńska, I. Yaremiy, A.T. Pędziwiatr, P. Kurzydło, B.F. Bogacz, and R. Gargula, *Ceram. Int.* 46, 27517 (2020).
67. P. Anantharamaiah, K. Manasa, and Y.S. Kumar, *Solid State Sci* 106, 106302 (2020).
68. V. Rathod, A.V. Anupama, R.V. Kumar, V.M. Jali, and B. Sahoo, *Vib. Spectrosc.* 92, 267 (2017).
69. A.R. Chavan, M. Babrekar, A.C. Nawle, and K.M. Jadhav, *J. Electron. Mater.* 48, 5184 (2019).
70. P. Anantharamaiah, and S. Giri, *Sens. Lett.* 18, 83 (2020).
71. A.B. Kulkarni, and S.N. Mathad, *Mater. Sci. Energy Technol.* 2, 455 (2019).
72. M. Meinert, and G. Reiss, *J. Phys. Conden. Matter* 26, 115503 (2014).
73. A. Kumar, R. Kumar, N. Verma, A.V. Anupama, H.K. Choudhary, R. Philip, and B. Sahoo, *Opt. Mater.* 108, 110163 (2020).
74. E.C. Devi, and I. Soibam, *J. Supercond. Novel Magn.* 31, 1183 (2018).
75. T.R. Tatarchuk, N.D. Paliychuk, M. Bououdina, B. Al-Najar, M. Pacia, W. Macyk, and A. Shyichuk, *J. Alloys Compd.* 731, 1256 (2018).
76. C. Himcinschi, I. Vrejoiu, G. Salvan, M. Fronk, A. Talkenberger, D.R. Zahn, D. Rafaja, and J. Kortus, *J. Appl. Phys.* 113, 084101 (2013).
77. A. Kalam, A.G. Al-Sehemi, M. Assiri, G. Du, T. Ahmad, I. Ahmad, and M. Pannipara, *Results Phys.* 8, 1046 (2018).
78. S. Perkowitz, *Optical characterization of semiconductors: infrared, Raman, and photoluminescence spectroscopy* (London: Elsevier, 2012).
79. M. Sultan, and R. Singh, *J. Appl. Phys.* 105, 07A512 (2009).
80. L. Zhang, G. Zheng, and Z.X. Dai, *J. Mater. Sci. Mater. Electron.* 27, 8138 (2016).
81. G.L. Jadhav, S. More, C. Kale, and K.M. Jadhav, *Physica B* 555, 61 (2019).
82. M.M.L. Sonia, S. Anand, V.M. Vinosel, M.A. Janifer, S. Pauline, and A. Manikandan, *J. Magn. Magn. Mater.* 466, 238 (2018).
83. V. Vinayak, P.P. Khirade, S.D. Birajdar, D. Sable, and K.M. Jadhav, *J. Supercond. Novel Magn.* 29, 1025 (2016).
84. V. Vasanthi, A. Shanmugavani, C. Sanjeeviraja, and R.K. Selvan, *J. Magn. Magn. Mater.* 324, 2100 (2012).
85. B.H. Devmunde, A.V. Raut, S.D. Birajdar, S.J. Shukla, D.R. Shengule, and K.M. Jadhav, *J. Nanopart.* 2016, 1 (2016).